Optics & Laser Technology 140 (2021) 107056

Contents lists available at ScienceDirect

Optics and Laser Technology

journal homepage: www.elsevier.com/locate/optlastec

Full length article

Mask-free patterning of Cu mesh as smart windows by spatially modulated nanosecond laser pulses

Qingwei Zhang [a], Donglin Huang [c], Dongfeng Qi [a,b,d,*], Wenju Zhou [a], Letian Wang [c], Zifeng Zhang [e], Songyan Chen [c], Shixun Dai [a], Hongyu Zheng [b,*]

[a] Laboratory of Infrared Materials and Devices, Ningbo University, Ningbo, Zhejiang Province 315211, People's Republic of China
[b] Center for Advanced Laser Manufacturing (CALM), Shandong University of Technology, Zibo, 255000, PR China
[c] Department of Physics, Xiamen University, Xiamen 361005, People's Republic of China
[d] Laser Thermal Laboratory, Department of Mechanical Engineering, University of California, Berkeley, Berkeley, CA 94720-1740, USA
[e] College of Mechanical and Electronic Engineering, Chaohu University, Hefei, Anhui 230000, People's Republic of China

ARTICLE INFO

Keywords:
Laser direct ablation
Spatially modulated
Copper mesh
Smart window

ABSTRACT

Laser direct fabrication of metallic mesh is a very promising structure for the next-generation transparent electrodes due to its outstanding optical and electrical properties. However, photoelectric properties and morphologies of the metallic mesh electrodes are not excellent after Gaussian pulse laser writing technology, which largely restricts the development of laser direct ablation process for the fabrication of high-quality transparent electrodes. In this study, we present newly developed copper mesh transparent electrode by spatially modulated one-step top-flat square nanosecond laser direct writing ablation of Cu film under ambient conditions. The copper square shaped electrode without outward radial mass transfer of molten metal, and no structural deformation and damage on the edge of metallic meshes. The clean square shaped of copper meshes structure not only shows high optical transparency in visual region and excellent a filtration in NIR regions, but also presents electrothermogenic of conductive copper mesh. In addition, the clean square shaped of copper mesh electrode on glass was demonstrated enhanced thermal shielding efficiency and defrost test as the smart windows.

1. Introduction

Metal patterned transparent electrode has aroused great concern in recent decades owing to its wide-ranging application in optoelectronics and energy devices [1–4]. Developing demand for higher reliability, beneficial portability and integration density of high-tech equipment's requires further plenty in the precision and quality of metal patterns [5]. The patterned copper mesh not only maintains the requirements of high transmittance and low cost of quartz or flexible substrate, but also reserves high conductivity, high thermal conductivity and ductility of copper film [6–8].

One of the most promising alternatives to fabricate the metal patterns transparent electrode is laser direct writing (LDW), which is atmospheric temperature and mask-free method of avoiding the restrictions of multi-process. LDW process can effectively fabricate grid structures in the surface of solution-processed nanoparticles (NPs) and thin films [9–12]. Compared with traditional processing methods, LDW process of metal grids of different pitches have unique advantage for the preparation of transparent electrodes. Due to metal films thinner than the light absorption depth is still conductive, and metal mesh making methods via laser ablation [6], laser sintering [10], reductive sintering [11] and pulsed irradiation [13] have been demonstrated for transparent electrodes.

However, the non-uniform morphology of the Gaussian short-pulse LDW electrode has led to poor electrical properties [6,14]. In the Gaussian beam, the temperature gradient in the spot causes different heat conduction processes in the center of the dot and the periphery of the dot, which affects the quality of the metal honeycomb transparent electrode [6,10,11]. Secondly, in the process of fabrication of metallic honeycomb electrode through pulsed laser ablation metal thin films, laser fluence at the peripheral of Gaussian spot is between the melting threshold and the ablation threshold of the material. In this case, the temperature gradient drives the molten material to the outer edge of the spot, and due to the solidification of the material transported after the laser pulse exposure, the cylindrical ring or wavy structure of droplets are formed in the peripheral melting zone. (The undulating structure is

* Corresponding authors at: Center for Advanced Laser Manufacturing (CALM), Shandong University of Technology, Zibo, 255000, PR China.
E-mail addresses: qidongfeng@sdut.edu.cn (D. Qi), zhenghongyu@sdut.edu.cn (H. Zheng).

https://doi.org/10.1016/j.optlastec.2021.107056
Received 12 April 2020; Received in revised form 22 October 2020; Accepted 3 March 2021
Available online 21 March 2021
0030-3992/© 2021 Elsevier Ltd. All rights reserved.

in excess of twice the original film thickness) [15]. The copper film is used as an oxygen-sensitive material. The Gaussian pulse LDW process will not only result in poor uniformity of the edge of the copper grid, but also the re-oxidized of the copper film will reduce the conductivity of the electrodes [15–17]. However, the thermal stress limiting characteristics of short wavelengths (UV) laser and the cold-working characteristics of ultrashort pulse (femtosecond) laser greatly reduce energy transfer, thereby avoiding heat accumulation [18,19]. But they have the drawback of being expensive. In this case, a further way would be utilizing deposition-processed copper films reconcilable with LDW ablation process to fabricate transparent electrode.

In this work, we present newly developed copper mesh transparent electrode by top-flat square nanosecond pulse LDW ablation of copper film under room temperature conditions. Nanosecond laser flat-top square spot doesn't have the outward radial transmission of molten metal, and will not cause deformation of the metal meshes electrode and damage to the edge. This clean square copper meshes structure shows high visible region transmittance (>85%) and outstanding a filtration in NIR regions. In addition, the copper mesh electrode on glass was demonstrated enhanced thermal shielding efficiency and defrost test as the smart windows application.

2. Material and methods

The laser direct writing (LDW) ablation process is schematically shown in Fig. 1a. The Nd: YVO_4 laser generates a nanosecond pulse laser, of which main parameters are as follows: 532 nm central wavelength, pulse width 22.5 ns, 1 kHz repetition rate and 2 W output average power. Upon irradiation of nanosecond laser pulses, a top-flat square beam can be modulated by a liquid crystal on silicon spatial light modulator (SLM: Throlabs-EXULUS-HD), resulting in the fabrication of square shaped arrays in copper film. The average reflectivity of the spatial light modulator we use is greater than 92%, and the diffraction efficiency is 86.05%. The power loss after passing through the spatial light modulator is less than 20.08%. The 4f system consisting of two convex lenses is used to reduce the beam of the laser and transmit the modulated laser from the SLM to the sample surface [20–22]. Then the top-flat beam was focused by through a 10 infinity-corrected objective lens, forming a top-flat focusing dot with a uniform luminance.

The top-flat beam was used to design a copper thin film, which was deposited on a quartz substrate by magnetron sputtering system. Cu films with different thickness were deposited on a silica (0.6 mm) substrate and polyethylene naphthalate (PEN: 0.12 mm) substrate via magnetron sputtering system, TRP-450 (Cr: current is 0.1 A, pressure is 0.6 Pa, and deposition time is 5 s. Cu: current is 0.3 A, chamber pressure is 0.5 Pa and deposition time is 160 s for 20 nm, 200 s for 50 nm and 400 s for 160 nm, respectively). The excellent adhesion between the Cu electrode and the substrate could be attributed to the thin (0.2–0.5 nm) chromium (Cr) adhesion layer. Fig. 1b shows separately one by one copper patterns on PEN substrates (5 cm × 10 cm) manufactured by LDW at the laser energy density of 210 mJ/cm^2. In order to illustrate the transmittance of the electrode, the photograph was taken with a printed pattern as a background. The electrode pattern can be adjusted through (computer-aided design) CAD system. Copper mesh electrode with different patterns at different stage shift control the moving speed of the sample is controlled by a linear stage (mode: KBD101 K-Cube, High Speed Translation of up to 500 mm/s, Resolution: 500 nm). As shown in Fig. 1c, the measured size of each shaped is approximately 30 μm, which is similar with the size of the beam spot. The experimental to measure laser beam intensity distribution using the knife on edge system in 2D. Moreover, the surface of the processed sample is clean and has no undulating structure, and the line width of the Cu grid is only 1 μm, as shown in the insert image. In this case, the Cu mesh not only has the superiority of the higher transparency but also maintains the good electronic conductivity of copper.

The scanning electron microscope (SEM: LEO 1530) system at 20 kV was used to characterize the surface morphology of the samples. Using the SPI4000/SPA-400 system running in tapping mode, and the surface structures were analyzed by AFM (atomic force microscopy). The temperature change of the sample surface was recorded by infrared camera (FLIR). The temperature test was carried out using a probe thermometer (jintuojia TA358) with an error range of ±0.1 °C.

3. Results and discussion

We focus on investigating the advantage of the top-flat square beam in fabrication of flexible transparent Cu mesh compared with Gaussian beam. The heat conduction mechanism of the substrate determines the optimal laser fluence [23]. In addition, the limited heat dissipation into thin film lowered thermal stress exerting on thermally ill-protected PEN substrates. After the LDW processing, the Cu film in the ablation areas is ejected, and the un-ablated parts of the film keep intact with outstanding adhesion to the substrate [6,14]. he ablation threshold fluence of LDW samples depends on the material irradiated by laser. Fig. 2 shows the SEM images of 20 nm, 50 nm and 160 nm copper films. For low laser fluence Gaussian beams (110 mJ/cm^2, 190 mJ/cm^2 and 290 mJ/cm^2),

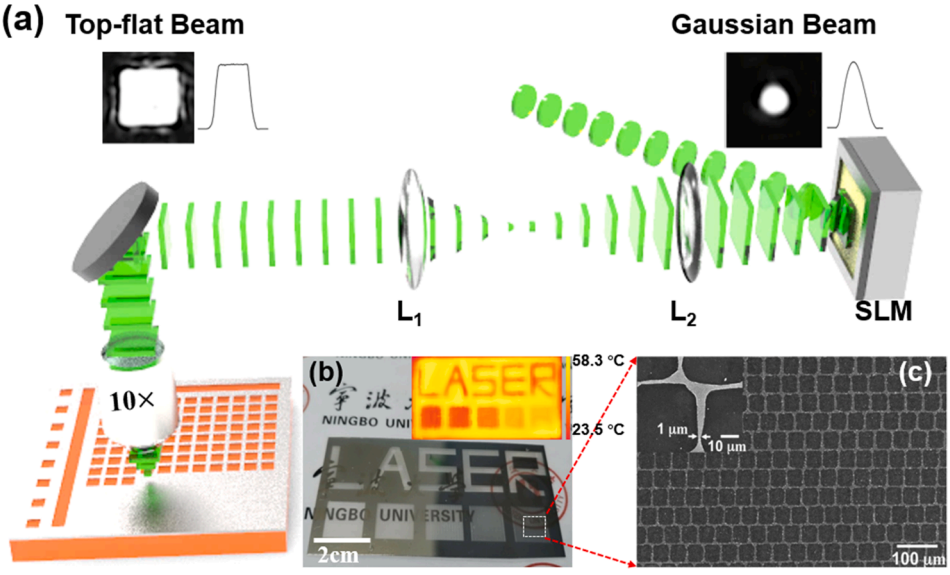

Fig. 1. (a) Fabrication schematics of Cu mesh smart windows. (b) Photograph of a transparent conductor on a PEN substrate (5 cm × 10 cm), and the background is the name of Ningbo University, the bottom five square areas (1.5 cm × 1.5 cm) are mesh patterns on the quartz substrate with different hole densities, and the insert image is thermal image of Cu metal mesh based transparent heater taken at 90 s after applying 6 V bias. (c) Top-view SEM image of Cu mesh-type (20 nm thickness) smart windows on the glass substrate. The inset shows the line-width of the Cu mesh is only 1 μm.

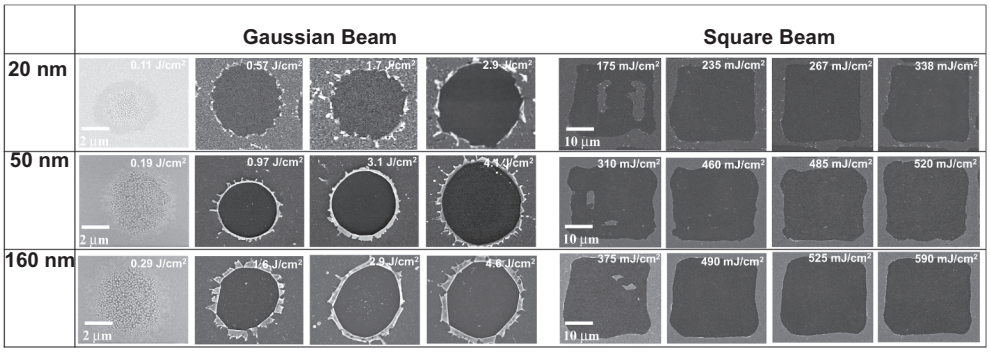

Fig. 2. SEM images indicate the characteristic stages of the morphological change of various thickness of Cu film (20 nm, 50 nm and 160 nm) on SiO_2 substrate under changing pulsed laser fluences.

droplet-like structures are formed in the central region, which means melting and dewetting. With the increase of irradiance fluence (0.57 J/cm^2, 0.97 J/cm^2 and 1.6 J/cm^2), the droplet-like structure in the center disappears, and the melted material is dewetting radially outward, which can also form droplet-like structure. At higher laser fluence, the peripheral edges and droplet fingerlike points appear around the circular grids. Ablation of thin Cu film typically brings abundant detritus and coarse surface morphology due to melt surface weakness and Gaussian beam with uneven energy. The top-flat square beam only has an incomplete ablation area, and no melting phenomenon occurs, and the detail SEM images are listed in Fig. 2. And if the laser energy density is lower than the threshold (197 mJ/cm^2, 397 mJ/cm^2 and 442 mJ/cm^2), the copper in the spot zone cannot be completely ablated. In this case, there is still some copper film residue inside the square cell. However, when the laser fluences at a higher level (in the ablation zone), the intensity of the beam zone can be uniform. Therefore, the top-flat square LDW ablation process can properly prevent the abundant debris and rough surface morphology problems. The square mesh structure can only be formed within the light spot, and the overall size does not change with the incident laser fluence. Moreover, since the fluence of the top-flat beam can mutate to zero at the edge of the beam spot, avoiding molten zone at the edge of the beam spot, in this case, there are not such abundant debris and rough surface morphology on Cu mesh.

Besides, the optimal value of laser flux depends not only on the heat transfer mechanism, but also on the thermal performance of the substrate [24]. In the theoretical simulation, the change trend of sample surface temperature with time and depth after LDW are studied, as described in Fig. 3. We assume that when the sample is irradiated, due to the rapid transfer of electron-photon energy, the photon energy is instantaneously and locally altered into heat. As shown in Fig. 3a, theoretical graph of surface temperature as a function of time after irradiation of Cu film with different laser pulse energy densities, 0.41 J/cm^2, 0.79 J/cm^2, 1.04 J/cm^2, respectively. The relevant laser pulse energy simulates the relationship between the temperature and depth of the stuff surface, as shown in Fig. 3a. When the copper film is light with sufficient energy laser, a melted area is constructed in the copper sample surface. Owing to the intense monochromaticity of the laser pulse, an intense transition is formed between the liquid phase and the solid phase in the ablation region. Since the diameter of the beam is greater than the length of absorption, we assume that the surface thermal radiation loss can be ignored. The heating spot irradiated by the laser to the sample surface is limited (30 μm), which is much larger than the film thickness (20 nm). Considering that ultra-fast deformation occurs on short notice, it is assumed that heat transfer and lattice deformation will not happen immediately in the direction perpendicular to the thickness [25]. The one-dimensional thermal diffusion differential equation of this process is as follows

$$C(T)\rho\frac{\partial T}{\partial t} = \alpha(1-R)I_0(t)exp^{-\alpha x} + \frac{\partial}{\partial x}(K(T)\frac{\partial T}{\partial x}) \quad (1)$$

In which, C(T), I_0(t), K(T), R and T = T(x t) are specific heat, the Gaussian laser (pulse: 532 nm, FWHM: 22.5 ns), thermal conductivity, reflectivity and temperature, respectively. T (x, 0) = T_0 is the initial condition, which shows the sample substrate temperature before laser irradiation. The Boundary conditions:

$$K_s\frac{\partial T}{\partial x}\Big|x_B - K_l\frac{\partial T}{\partial x}\Big|x_B = L\frac{\partial x_B}{d_t} \quad (2)$$

$$x = 0, \frac{\partial T}{\partial x} = 0 \quad (3)$$

$$x\to\infty, T - T_0 \quad (4)$$

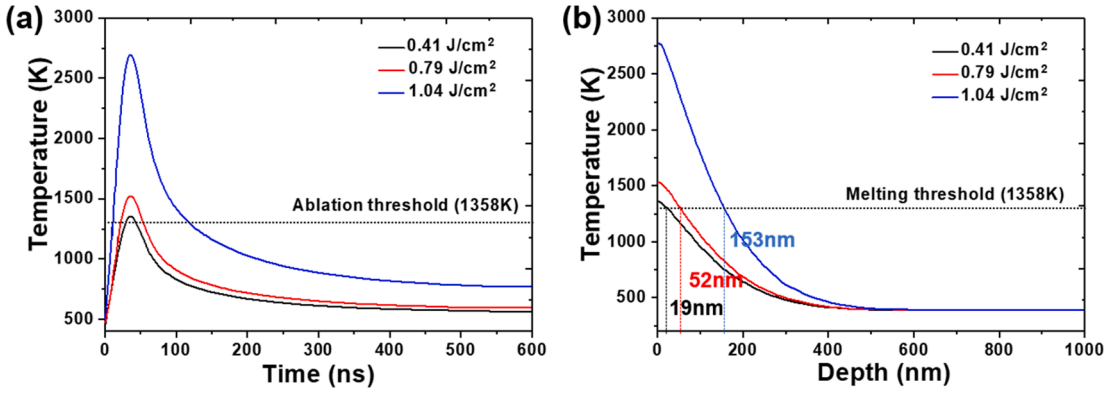

Fig. 3. Under different laser energy densities, (a) the relationship of the temperature of the copper film surface with time. (b) The relationship between temperature and depth.

In Eq. (2)–(4), s and l are solid and liquid, L is the latent heat of fusion, and x is the position of the liquid-solid transition. The Eq. (2) shows the heat transfer when the copper material converts from a solid phase to a liquid phase. From the Eq. (3), it is considered that the heat loss on the sample surface can be ignored. According to the temperature model calculation, the following parameters can be estimated, such as the melting time and depth of the sample and the surface temperature of the sample. The thermo-optical data used in the calculation of the temperature model are provided by references [26,27], as shown in Table 1. In this condition, the ablation depths of copper (532 nm) with different fluences are calculated. Since the thickness of the copper film (20 nm, 50 nm and 160 nm) was similar with that of the ablation depth (19 nm, 52 nm and 153 nm), and the laser energy was almost completely absorbed by the copper sample, as shown in Fig. 3b. In addition, the effective absorption of thermal radiation by the Cu thin film greatly reduces the thermal stress applied to the PEN substrate [28]. After the LDW processing, the Cu film in the ablation areas is ejected, and the unablated portion of the film remains intact and exhibits excellent adhesion. Ablation caused by laser direct writing is related to the laser energy density, which mainly depends on the laser used and the material.

In addition, the AFM image shows that the morphology between the film and the ablated holes after Gaussian and top-flat square beam irradiation, as shown in Fig. 4c. For the Gaussian beam LDW ablation processing, the original thickness of the copper mesh electrode measured by AFM is approximately 20 nm. Because of the intense melt expulsion and ablation, condensed and re-solidified copper clusters are found near the peripheries of the holes. Furthermore, the border of the ablated holes is around two times thicker than the original film, meaning outward radial mass transfer of molten metal, as shown in Fig. 4a. For LDW ablation processing, the rim droplet fingers will not appear in the edge of the spot, and the inner hole is smooth and neat, as shown in Fig. 4c. It is worth noting that the edges of the top-flat square LDW ablation electrode mesh are sharp, suggesting that this top-flat square LDW ablation process can be applied to a high-resolution electrode fabrication, as shown in Fig. 4a. In this case, upon the top-flat square ns LDW ablation, square copper cell arrays can be produced in a copper film on a flexible PEN substrate, which can maintain good conductivity and improve transparency. Besides the advantage of the top-flat LDW ablation processing for the fabrication of Cu mesh electrode, square cell arrays can effectively reduce the areal densities according to the circle cell arrays (from 0.48 to 0.27). The areal density is herein defined as the ratio of the metal coverage area after ablation to the total area. For samples with an area of 2 cm * 2 cm, the corresponding scanning speed and time under different areal densities are shown in Table 2. By changing the scanning speed and jog step size, cell arrays with different areal densities can be maintained. For the square arrays, the areal density can be fabricated as high as 0.27. However, the areal density of circle arrays is only 0.48. The lower areal density result in the higher transparency, in this condition, compare with the Gaussian beam LDW processing, the top-flat square LDW ablation processing can not only maintain Cu mesh with higher electrical conductivity but also higher transparency, which can be defined as cold machining technology.

The copper film was subjected to square ns LDW ablation, and the copper mesh electrode was prepared by a rapid cold working process under room temperature. In this case, there are no such molten materials, the cylindrical ring structures forms in the peripheral dewetting zone and no re-oxidized metallic materials appear after laser irradiation. The smoothness of the copper mesh electrode not only increases the photoelectric performance, but also reduces the heat leakage of the electric heater, which greatly improves the development of the LDW ablation process for manufacturing high-quality electrodes [15–17]. In order to study the effect of voltage on the copper mesh heater, temperature curves of copper mesh heaters with time under different voltages are given. Fig. 5a shows the temperature-time curves of Cu mesh film heaters with different copper thickness (areal density:0.37) under the voltage of 3.5 V. When the thickness of copper mesh is 20 nm, no obvious temperature change is observed, which indicates that the thickness of copper has a great influence on the temperature change. As the temperature increases, the film heater can reach a steady-state temperature within 50 s, as shown in Fig. 5a. As the copper thickness concentration increases from 20 nm to 160 nm, the steady-state temperature rises from 45.5 °C to 85.2 °C. Fig. 5b presents the temperature augmentation of the heater recorded by an IR camera from 1 to 4 V (0.5 V every 60 s). The steady-state temperature ranged from 22.1 to 77.1 °C, showing that the temperature of the copper mesh sample increases with the increase of voltage. It is indicated that the transparent electrode after the DC voltage is applied had good conductivity.

Smart window is a kind of functional device, it can integrate heating defogging and infrared heat shielding. The excellent conductivity and heat transfer performance of the copper mesh transparent electrode show that it can be used in mist eliminator. The measurement of visible and infrared transmittance proves that the electrode can be used as an application material for infrared heat shielding. As shown in Fig. 6a, the optical characteristics of the smart window from the visible area to the infrared area are given. With the increase of the area density, the transmittance increases gradually, and the transmittance in the infrared region is lower than that in the visible region. Due to the adjustable linewidth between the mesh, the Cu mesh with smaller area density can be obtained. As shown in Fig. 6b, the photoelectric performance comparison of the copper grid transparent electrode obtained by different preparation methods is given. Among the optimal results, the copper grid electrode fabricated by square beam processing has better photoelectric performance (high transmittance 85.1% at 550 nm with low sheet resistance 15.2 Ω/sq), as shown in the inset. Furthermore, metal materials (Cu mesh) which transmissions narrow bandwidths of light, mostly in the visible region. These materials could be adjusted to interact in the infrared region. Therefore, the copper mesh electrode can well achieve the function of shielding infrared (thermal). To evaluate the response temperature condition for thermal shielding smart window, an infrared baking lamp, a little house, a temperature sensor, and Cu mesh smart window are utilized, as depicted in Fig. 6e. A right window of the house held a temperature sensor. The Cu mesh smart window device was established on the roof of the mock-up model house, and the baking lamp was placed top the smart window to simulate the scene of sunlight. Fig. 6b shows the results of in situ temperature monitoring on Cu mesh smart windows. For validation of the shielding efficiency, we mounted Cu mesh smart windows and commercial silica glass onto the model house. The infrared bulb of the infrared baking lamp has a capacity of 100 W, which can produce a light of 2 W/cm^2 similar to the solar spectrum. Without outside interference, the house temperature in the laboratory showed 23.8 °C. As shown in Fig. 6e, after 10 min of exposure under the light irradiation of a baking lamp, the measured temperature was increased up to 38.9, 33.8, 31.6 °C and 30.6 °C for the model house with 0, 0.37, 0.54 and 0.77 area density copper mesh electrode. A curve in Fig. 6d shows, comparing with the silica glass ($\Delta T = 15.2$ °C), the indoor temperature with 0.77 copper mesh area density electrode on glass slowly increases ($\Delta T = 6.8$ °C), and even the ΔT of 0.37 copper mesh area density electrode on glasses only 10 °C. This shows that the Cu mesh electrode smart window has a great

Table 1
Parameters for Cu used in ablation depth calculation.

Cu (Parameters)	Values
Initial temperature (T_0)	300 K
Thermal conductivity (k)	401 W·m^{-1}·K^{-1}
Electron heat capacity (C_l)	99.6T_eJ·m^{-3}·K^{-1}
Lattice heat capacity (C_e)	3.5 × 10^6 J·m^{-3}·K^{-1}
Absorption coefficient (α)	7 × 10^7 m^{-1}
Density (ρ)	8.96 g·cm^{-3}
Reflection coefficient (R)	0.6
Melting point	1358 K

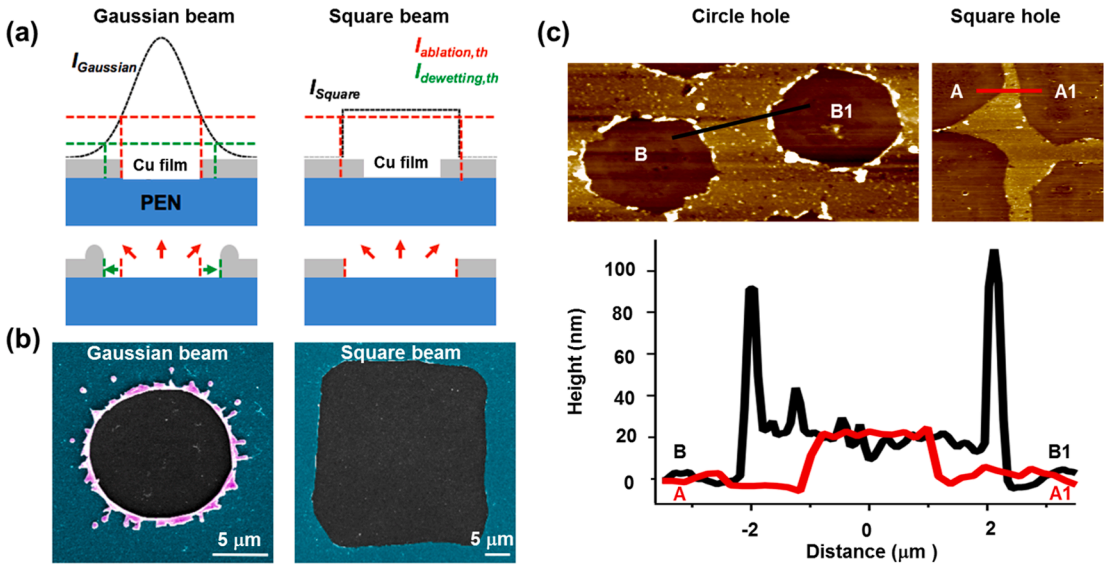

Fig. 4. (a) Schematics of morphology transformations of Cu film upon Gaussian LDW ablation processing and ultrathin Cu film upon top-flat square LDW ablation processing. $I_{Gaussian}$ and I_{Square} are the laser intensity profiles for the Gaussian laser beam and the top-flat square laser beam, respectively. The intensity profile is presented with a dashed line. The solid arrows indicate the transport directions of molten copper upon the laser irradiation. (b) The typical SEM images of the corresponding 20 nm copper film on PEN substrate after Gaussian beam and top-flat square LDW ablation processes, and fluences of the irradiation laser 1.44 J/cm^2 for Gaussian beam, and 490 mJ/cm^2 for top-flat square beam, and the scale bars are 5 μm. (c) AFM image of the copper electrode.

Table 2
Scanning speed and time for different areal densities.

Areal density	Velocity	Jog step size	Time
0.37	37.8 mm/s	37.8 μm	4.7 min
0.54	44.2 mm/s	44.2 μm	3.4 min
0.77	62.5 mm/s	62.5 μm	1.76 min

effect on infrared thermal shielding. In addition, the transmittance and conductivity of the Cu metallic mesh electrode enable the fabrication of the smart window for defrost test. A defrost test was used to further demonstrate copper mesh transparency electrode heater performance. As shown in Fig. 6(f-g), a defrost block with an area of 30 × 30 mm was placed on the mesh-free surface (copper mesh area density: 0.37, size: 30 × 30 mm). We can control the horizontal moving speed (38 mm/s) and the step size (0.038 mm) of the linear displacement table to obtain the Cu mesh electrode. Fig. 6f shows the image temperature processing of the inverter under 7.5 V DC voltage input under different heating times. The maximum temperature is as high as 105 °C in 60 s, which shows that the flexible transparent electrode has strong thermal sensitivity. Before heating with the copper mesh electrode heaters, the background word under the smart window cannot be observed. Fig. 6g provides an intuitive defogging effect diagram, and the water mist attached to the sample is continuously reduced over time. After 30 s, the background image gradually becomes clear, but the water mist still exists on the sample. At 60 s, the remaining droplets fully evaporated, and the words "Ningbo University" can be seen clearly in the background. In addition, we monitor the tolerance of the samples at room temperature, and the earliest prepared samples have been stored for 200 days. The sheet resistance (15.2 Ω/sq) change is updated as shown in Fig. 6c. Besides, to verify whether the copper mesh transparent electrode is oxidized before and after defogging, we show the XRD measurement results under each sheet resistance in Fig. 6c. The XRD peak at 43.3° corresponds to Cu (1 1 1). The peaks of Cu_2O and CuO did not appear in the figure, indicating that the Cu mesh transparent electrode after defogging treatment was not oxidized. Therefore, defrost test and portable heating with a 7.5 V DC prove the possibility of using the Cu mesh for vehicle defrosting [29], and other areas [30,31].

4. Conclusion

In conclusion, we introduced advanced top-flat LDW technologies to manufacture the copper square shaped mesh electrode without outward

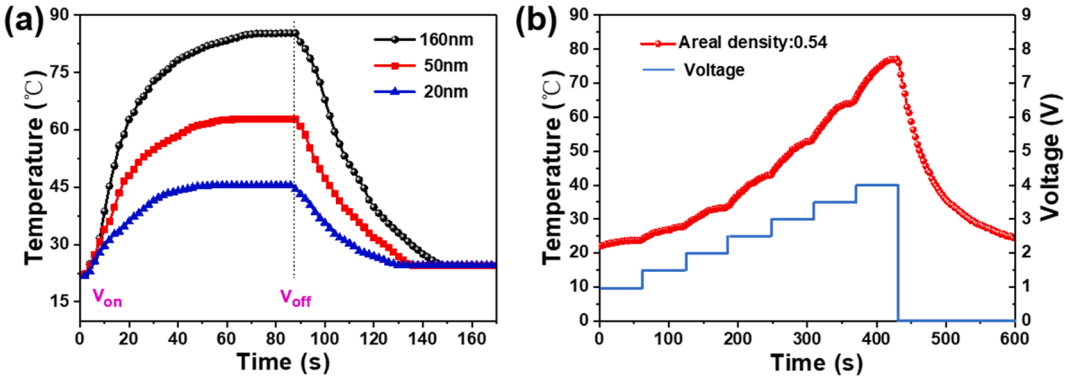

Fig. 5. (a) Temperature-time profiles of the Cu mesh heaters under different thickness, 3.5 V DC voltage. (b) The temperature augmentation of the heater recorded by an IR camera from 1 to 4 V (0.5 V every 60 s).

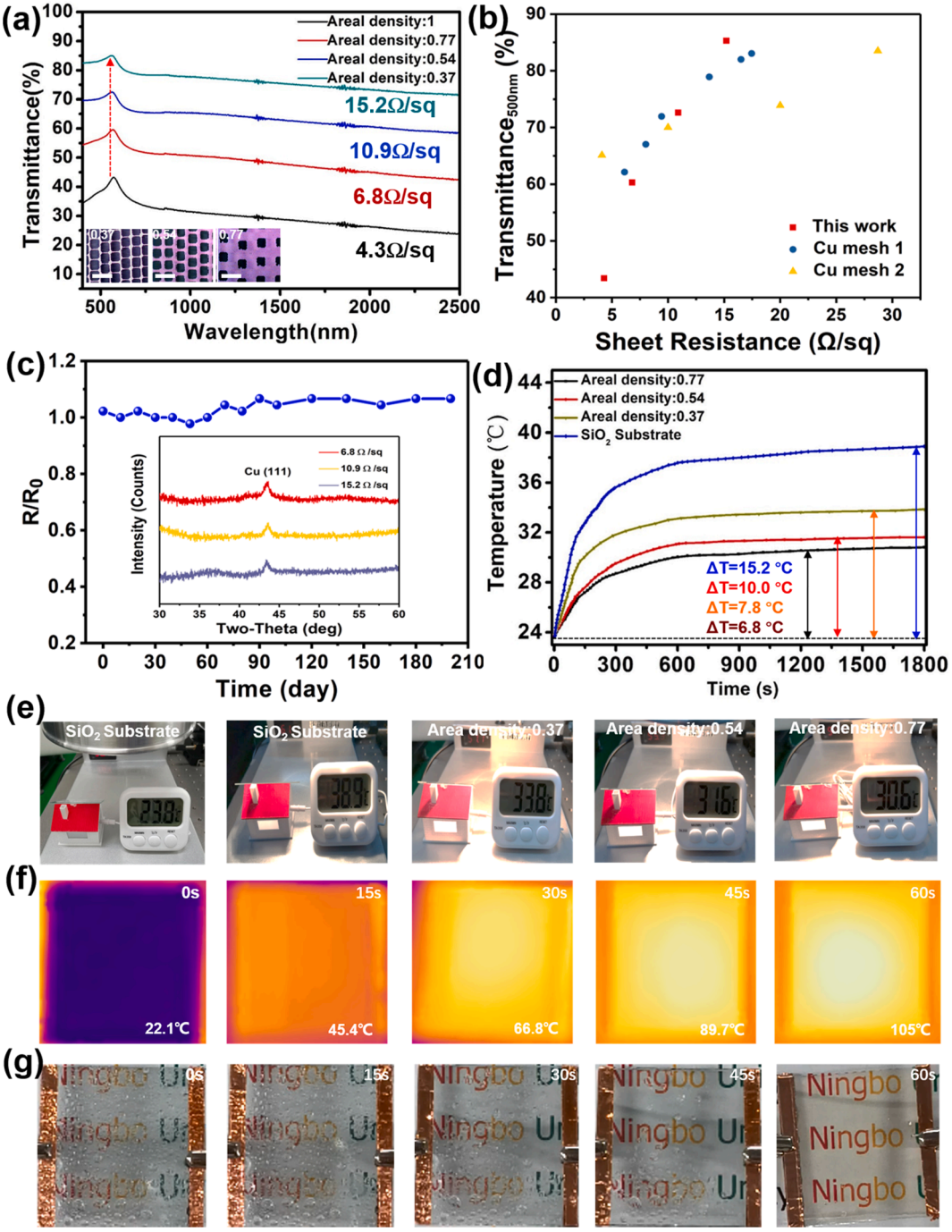

Fig. 6. (a) Vis-NIR transmittance with respect to Cu mesh smart windows under different area densities, and the scale bars in the optical images are all 100 m. (b) Comparison of photoelectric performance of three copper mesh transparent electrodes. (c) The rate of change of the sheet resistance of the 15.2 Ω/sq sample in 200 days. The inset is the XRD test chart of the copper grid after defogging under different square resistances. (d) Changes of the interior air temperature in the model building with the SiO_2 glass and Cu mesh electrode smart windows as a function of time under light irradiation of an infrared baking lamp. (e) Monitoring of in situ temperature change of the Cu mesh smart windows with different area densities on the model building. (f) Use FLIR to process images with the temperature of the heater under a DC voltage input of 7.5 V under different heating times. (g) Demonstration of transparent Cu mesh smart windows heater performance, and the water evaporation test with 7.5 V operating voltage was performed.

radial mass transfer of molten metal, resulting in no structural deformation and damage on the edge of metallic meshes. The resistance and transmittance of the copper electrode can be easily controlled by adjusting the surface copper hole area density. This clean square copper meshes structure showed high optical transparency in visual region and excellent a filtration in NIR regions, which can be used as thermal shielding window. On the other hand, a transparent heater based on the electrothermogenic of conductive copper mesh exhibited excellent exothermic properties. In this condition, the copper mesh electrode on glass was demonstrated enhanced thermal shielding efficiency and defrost test as the next-generation smart windows.

Author contributions

Qingwei Zhang designed the experiment; carried out nano-fabrication, laser processing, and characterization; as well as analyzed

the results. Dongling Huang contributed in carrying out SEM analysis. Wenju Zhou and Letian Wang offered critical suggestions on the result summary of this work. Zifeng Zhang helped and guided the nano-fabrication. Songyan Chen assisted in demonstrating patterns. ShiXun Dai built the processing setup. Hongyu Zheng offered helpful discussions on thermal analysis. Dongfeng Qi supervised and supported the work.

Declaration of Competing Interest

The authors declare that they have no known competing financial interests or personal relationships that could have appeared to influence the work reported in this paper.

Acknowledgements

This work was supported by the National Natural Science Foundation of China (61705117); Natural Science Foundation of Ningbo (2018A610043); and Chinese Scholars Council. And acknowledge the support of 3315 innovation team, Ningbo city. It was also support by K. C. Wong Magna Fund in Ningbo University.

References

[1] P. Sopeña, J. Arrese, S. González-Torres, J.M. Fernández-Pradas, A. Cirera, P. Serra, Low-cost fabrication of printed electronics devices through continuous wave laser-induced forward transfer, ACS Appl. Mater. Interfaces 9 (2017) 29412–29417.
[2] B. Kang, S. Han, J. Kim, S. Ko, M. Yang, One-step fabrication of copper electrode by laser-induced direct local reduction and agglomeration of copper oxide nanoparticle, J. Phys. Chem. C 115 (2011) 23664–23670.
[3] D. Konios, C. Petridis, G. Kakavelakis, M. Sygletou, K. Savva, E. Stratakis, E. Kymakis, Reduced graphene oxide micromesh electrodes for large area, flexible, organic photovoltaic devices, Adv. Funct. Mater 25 (2015) 2213–2221.
[4] M. Theuring, V. Steenhoff, S. Geißendörfer, M. Vehse, K. von Maydell, C. Agert, Laser perforated ultrathin metal films for transparent electrode applications, Opt. Express 23 (2015) A254–A262.
[5] P. Sopeña, P. Serra, J. Fernández-Pradas, Transparent and conductive silver nanowires networks printed by laser-induced forward transfer, Appl. Surf. Sci. 476 (2019) 828–833.
[6] D. Paeng, J.H. Yoo, J. Yeo, D. Lee, E. Kim, S.H. Ko, C.P. Grigoropoulos, Low-cost facile fabrication of flexible transparent copper electrodes by nanosecond laser ablation, Adv. Mater. 27 (2015) 2762–2767.
[7] A. Wang, L. Jiang, X. Li, Y. Liu, X. Dong, L. Qu, X. Duan, Y. Lu, Mask-free patterning of high-conductivity metal nanowires in open air by spatially modulated femtosecond laser pulses, Adv. Mater. 27 (2015) 6238–6243.
[8] T. Wang, L.-C. Jing, Q. Zhu, A.S. Ethiraj, Y. Tian, H. Zhao, X.-T. Yuan, J.-G. Wen, L.-K. Li, H.-Z. Geng, Fabrication of architectural structured polydopamine-functionalized reduced graphene oxide/carbon nanotube/PEDOT: PSS nanocomposites as flexible transparent electrodes for OLEDs, Appl. Surf. Sci. 500 (2020) 143997.
[9] S. Hong, H. Lee, J. Yeo, S.H. Ko, Digital selective laser methods for nanomaterials: From synthesis to processing, Nano Today 11 (2016) 547–564.
[10] S. Hong, J. Yeo, G. Kim, D. Kim, H. Lee, J. Kwon, H. Lee, P. Lee, S.H. Ko, Nonvacuum, maskless fabrication of a flexible metal grid transparent conductor by low-temperature selective laser sintering of nanoparticle ink, ACS Nano 7 (2013) 5024–5031.
[11] D. Lee, D. Paeng, H.K. Park, C.P. Grigoropoulos, Vacuum-free, maskless patterning of Ni electrodes by laser reductive sintering of NiO nanoparticle ink and its application to transparent conductors, ACS Nano 8 (2014) 9807–9814.
[12] D.J. Joe, S. Kim, J.H. Park, D.Y. Park, H.E. Lee, T.H. Im, I. Choi, R.S. Ruoff, K. J. Lee, Laser–material interactions for flexible applications, Adv. Mater. 29 (2017) 1606586.
[13] B. Yoo, Y. Kim, C.J. Han, M.S. Oh, J.-W. Kim, Recyclable patterning of silver nanowire percolated network for fabrication of flexible transparent electrode, Appl. Surf. Sci. 429 (2018) 151–157.
[14] D. Qi, D. Paeng, J. Yeo, E. Kim, L. Wang, S. Chen, C.P. Grigoropoulos, Time-resolved analysis of thickness-dependent dewetting and ablation of silver films upon nanosecond laser irradiation, Appl. Phys. Lett 108 (2016) 211602.
[15] D. Paeng, J. Yeo, D. Lee, S.-J. Moon, C.P. Grigoropoulos, Laser wavelength effect on laser-induced photo-thermal sintering of silver nanoparticles, Appl. Phys. A 120 (2015) 1229–1240.
[16] D. Paeng, D. Lee, J. Yeo, J.-H. Yoo, F.I. Allen, E. Kim, H. So, H.K. Park, A.M. Minor, C.P. Grigoropoulos, Laser-induced reductive sintering of nickel oxide nanoparticles under ambient conditions, J. Phys. Chem. C 119 (2015) 6363–6372.
[17] D. Paeng, D. Lee, C.P. Grigoropoulos, Characteristic time scales of coalescence of silver nanocomposite and nanoparticle films induced by continuous wave laser irradiation, Appl. Phys. Lett 105 (2014) 073110.
[18] B. Liu, Z. Hu, Y. Che, Y. Chen, X. Pan, Nanoparticle generation in ultrafast pulsed laser ablation of nickel, Appl. Phys. Lett. 90 (2007) 044103.
[19] K. Takahashi, M. Tsukamoto, S. Masuno, Y. Sato, Heat conduction analysis of laser CFRP processing with IR and UV laser light, Compos. Part A-Appl. Sci. Manuf. 84 (2016) 114–122.
[20] L. Zhu, J. Wang, Arbitrary manipulation of spatial amplitude and phase using phase-only spatial light modulators, Sci. Rep. 4 (2014) 7441.
[21] R.J. Beck, J.P. Parry, W.N. MacPherson, A. Waddie, N.J. Weston, J.D. Shephard, D. P. Hand, Application of cooled spatial light modulator for high power nanosecond laser micromachining, Opt. Express 18 (2010) 17059–17065.
[22] K. Osawa, M. Yoshida, Y. Nakata, N. Miyanaga, A. Narazaki, T. Shoji,Y. Tsuboi In Beam shaping by spatial light modulator and 4f system to square and top-flat for interference laser processing, Laser Applications in Microelectronic and Optoelectronic Manufacturing (LAMOM) XXII, International Society for Optics and Photonics, 2017, p 100911C.
[23] K. Furusawa, K. Takahashi, H. Kumagai, K. Midorikawa, M. Obara, Ablation characteristics of Au, Ag, and Cu metals using a femtosecond Ti: sapphire laser, Appl. Phys. A 69 (1999) S359–S366.
[24] B.N. Chichkov, C. Momma, S. Nolte, F. Von Alvensleben, A. Tünnermann, Femtosecond, picosecond and nanosecond laser ablation of solids, Appl. Phys. A 63 (1996) 109–115.
[25] J.K. Chen, J.E. Beraun, L.E. Grimes, D.Y. Tzou, Modeling of femtosecond laser-induced non-equilibrium deformation in metal films, Int. J. Solids Struct. 39 (2002) 3199–3216.
[26] H. Elsayed-Ali, T. Norris, M. Pessot, G. Mourou, Time-resolved observation of electron-phonon relaxation in copper, Phys. Rev. Lett. 58 (1987) 1212.
[27] P. Corkum, F. Brunel, N. Sherman, T. Srinivasan-Rao, Thermal response of metals to ultrashort-pulse laser excitation, Phys. Rev. Lett. 61 (1988) 2886.
[28] E.G. Gamaly, N. Madsen, M. Duering, A.V. Rode, V.Z. Kolev, B. Luther-Davies, Ablation of metals with picosecond laser pulses: evidence of long-lived nonequilibrium conditions at the surface, Phys. Rev. B 71 (2005) 174405.
[29] S.-S. Yoon, D.-Y. Khang, Facile patterning of Ag nanowires network by micro-contact printing of siloxane, ACS Appl. Mater. Interfaces 8 (2016) 23236–23243.
[30] T.H. Park, S. Yu, M. Koo, H. Kim, E.H. Kim, J.-E. Park, B. Ok, B. Kim, S.H. Noh, C. Park, Shape-adaptable 2D titanium carbide (MXene) heater, ACS Nano 13 (2019) 6835–6844.
[31] M. Cao, M. Wang, L. Li, H. Qiu, Z. Yang, Effect of graphene-EC on Ag NW-based transparent film heaters: optimizing the stability and heat dispersion of films, ACS Appl. Mater. Interfaces 10 (2018) 1077–1083.